



Tetrameric PilZ protein stabilizes stator ring in complex flagellar motor and is required for motility in *Campylobacter jejuni*

Yuanyuan Chen^{a,b,c,d,1} , Shoichi Tachiyama^{e,f,1} , Yuqian Li^{a,b,c} , Xueyin Feng^{a,b,c,d} , Hang Zhao^{e,f,g}, Yanmin Wu^{a,b,c,d} , Yu Guo^{a,b,c}, María Lara-Tejero^e, Canfeng Hua^e, Jun Liu^{e,f} , and Beile Gao^{a,b,c,2}

Affiliations are included on p. 10.

Edited by Qijing Zhang, Iowa State University, Ames, IA; received July 1, 2024; accepted November 19, 2024

Rotation of the bacterial flagellum, the first identified biological rotary machine, is driven by its stator units. Knowledge gained about the function of stator units has increasingly led to studies of rotary complexes in different cellular pathways. Here, we report that a tetrameric PilZ family protein, FlgX, is a structural component underneath the stator units in the flagellar motor of *Campylobacter jejuni*. FlgX forms a stable tetramer that does not bind cyclic di-GMP (c-di-GMP), unlike other canonical PilZ domain-containing proteins. Cryoelectron tomography and subtomogram averaging of flagellar motors in situ provide evidence that FlgX interacts with each stator unit and plays a critical role in stator ring assembly and stability. Furthermore, FlgX is conserved and was most likely present in the common ancestor of the phylum *Campylobacterota*. Overall, FlgX represents a divergence in function for PilZ superfamily proteins as well as a player in the key stator–rotor interaction of complex flagellar motors.

Campylobacter | PilZ | stator | flagella | motility

Flagellar motility in bacteria is energized by ion motive force consumed by stator units made of two proteins: MotA and MotB (1, 2). Studies of the flagellar motor, the first biological rotary machine discovered, have greatly improved our knowledge of molecular rotation (3). In addition, the broad impact of this knowledge on microbiology stems from homology between MotAB and ExbBD/TolQR/GldLM/AglQRS/ZorAB, which form similar rotary complexes (4–10). The latter complexes are involved in cellular processes, including nutrient uptake, cell division, gliding motility, and phage defense, indicating a much broader role for rotary complexes in bacterial cells (10–14).

Recently, major advances have been made toward a working model of stators in the context of the flagellar motor (15, 16). First, single-particle cryoelectron microscopy (cryo-EM) studies updated the stoichiometry of the stator unit as a 5:2 rotary complex (MotA₅B₂) (4, 5). Second, in situ cryoelectron tomography (cryo-ET) and cryo-EM studies revealed unprecedented details of stator–rotor interaction (17–21). And third, beyond the model organisms *Escherichia coli* and *Salmonella enterica*, many other species have additional periplasmic scaffolds in their motors that stabilize and form a wider stator ring to generate higher torque (22–25). Examples include the H- and T-rings in *Vibrio* spp. (26, 27), collar structure in *Borrelia burgdorferi* (28–30), and basal/medial/proximal disks in *Campylobacter jejuni* and *Helicobacter pylori* (23, 24).

In the current “wheels with wheels” model of the flagellar motor, stator units as small active cogs drive rotation of a large passive cog, the C-ring (1, 2, 15). In each stator unit, the MotA pentamer rotates around the MotB dimer with support from the periplasmic FliL ring, which stabilizes the stator unit in an extended, active conformation (31, 32). FliL rings in nearly all motors and additional periplasmic scaffolds in complex motors are believed to be static in the periplasm during motor rotation (31–33). To date, no cytoplasmic proteins have been reported that form a stable complex with the stator unit in bacteria, although some motility regulatory proteins, such as YcgR/MotI, may interact dynamically with MotA (34, 35). Moreover, no proteins are known to rotate with individual stator units encircling their dimeric axle.

Our previous Tnseq screening for motility genes in *C. jejuni* identified a protein, FlgX, required for flagellar motility but not for filament assembly (36). In addition, FlgX coimmunoprecipitated with both MotA and MotB in *C. jejuni* cell lysates (36). FlgX affects the stability of both MotA and MotB, likely through direct interaction with MotA, and localizes exclusively to the cytoplasm (37). Suppressor analysis of a Δ flgX mutant identified several motility suppressor mutations in the *motAB* operon or *ftsH*, and FtsH is a protease that assists the quality control of inner membrane proteins (37). Hence, FlgX has been proposed as a chaperone for stator units, though it remains unknown whether FlgX is

Significance

Stator units are key components in the flagellar motor. In the current “wheels with wheels” model, the stator units are small active cogs that drive rotation of a large passive cog and, in turn, rotation of the extracellular filament. Here, we report that FlgX, a member of the tetrameric PilZ family, forms an elongated tetramer interacting with the cytoplasmic region of each stator unit and stabilizing the stator ring formed by 17 stator units in *Campylobacter jejuni*. The specific location of the FlgX tetramer adds complexity to our understanding of stator–rotor interaction. Importantly, FlgX plays a structural, rather than regulatory, role in the flagellar motor, shedding light on the functional versatility of the ancient PilZ superfamily.

Author contributions: B.G., S.T., and J.L. designed research; Y.C., S.T., Y.L., X.F., H.Z., Y.W., Y.G., and C.H. performed research; M.L.T. provided samples; Y.C., S.T., J.L., and B.G. analyzed data; and Y.C., S.T., J.L., and B.G. wrote the paper.

The authors declare no competing interest.

This article is a PNAS Direct Submission.

Copyright © 2024 the Author(s). Published by PNAS. This article is distributed under Creative Commons Attribution-NonCommercial-NoDerivatives License 4.0 (CC BY-NC-ND).

¹Y.C. and S.T. contributed equally to this work.

²To whom correspondence may be addressed. Email: gaob@scsio.ac.cn.

This article contains supporting information online at <https://www.pnas.org/lookup/suppl/doi:10.1073/pnas.2412594121/-/DCSupplemental>.

Published December 30, 2024.

released after chaperone activity or incorporated into the flagellar motor (37).

The PilZ domain is a widespread receptor for c-di-GMP, a secondary messenger with a regulatory role in flagellar motility (38, 39). Several PilZ domain-containing proteins in different species control flagellar motility in a c-di-GMP-dependent manner (40, 41). The best-studied example, the two-domain protein YcgR in *E. coli*, serves as a brake for flagellar rotation (34, 42), while its homolog MotI in *Bacillus subtilis* acts as a clutch to inhibit motility (35), and other homolog FlgZ in *Pseudomonas aeruginosa* impacts swarming via interactions with stator protein MotC (41). The second type of PilZ family proteins contains only one canonical PilZ domain, such as MapZ in *P. aeruginosa* that interacts with chemotaxis protein CheR to control flagellar motor switching (43) and MotL in *Shewanella putrefaciens* that specifically regulates the activity of the secondary lateral flagellar system (44). All of the above PilZ domain-containing proteins can bind c-di-GMP in a reversible manner to dynamically interact with flagellar or chemotaxis proteins. Finally, a third type—called tetrameric PilZ (tPilZ)—contains an atypical PilZ domain with two extra alpha helices and forms stable tetramers (45). Beyond structural information, the function of tPilZ proteins has remained unknown.

Here, we find that FlgX belongs to the tPilZ family and forms a stable tetramer that does not bind c-di-GMP. Cryo-ET studies suggest that FlgX interacts with the cytoplasmic part of the MotA pentamer, stabilizing the stator ring formed by 17 stator units in *C. jejuni*. Lack of FlgX results in loss of stator units, incomplete formation of the FlgL ring, and loss of adjacent densities bridging two FlgX complexes. Last, FlgX coevolved with the ancestral flagellar gene set and F3 chemosensory class in the phylum *Campylobacterota*. Taken together, these findings reveal that FlgX plays a critical role in structure and function of the *C. jejuni* flagellar motor, representing a divergence of PilZ superfamily proteins.

Results

FlgX Belongs to the tPilZ Family. Searching for homologs of FlgX (CJJ81176_0199, Accession No.: WP_002854663.1) against the NCBI nonredundant protein database only returned protein hits from species of the phylum *Campylobacterota*, which led us to conclude that FlgX is restricted to *Campylobacterota* (previously called *epsilonproteobacteria*) (36). All identified proteins are 160 to 190aa in length, with no identifiable domain or motif (SI Appendix, Table S1). Surprisingly, both HHpred and AlphaFold analyses of FlgX show with high confidence that it is structurally similar to the tPilZ protein XCC6012 from *Xanthomonas campestris* even though their shared sequence identity is as low as 6% (Fig. 1 A and B and SI Appendix, Fig. S1) (45).

Structure-guided sequence alignment revealed that FlgX shares almost all characteristics of tPilZ revealed by studies of XCC6012 and other tPilZ domain-containing proteins: 1. a six-stranded β -barrel flanked by three helices, missing only the N terminus α 1; 2. two additional long helices, α 2 and α 3, between the β 1 and β 2 strands and unique to tPilZ but absent from the canonical PilZ domain; 3. conserved hydrophobic residues in β 1/ β 2/ β 3/ β 4/ β 5/ β 6 that form the hydrophobic pocket and determine the core β -barrel fold; and 4. conserved hydrophobic residues in α 3 important for tetramer formation (Fig. 1 A and B and SI Appendix, Fig. S1) (38, 45). Note that conservation here means that the positions of hydrophobic residues are well conserved, while the residues themselves vary (Fig. 1A) (38).

To test the oligomerization status of FlgX, size-exclusion chromatography coupled with multiangle light scattering (SEC-MALS) was performed. The measured molar mass of the FlgX protein was 81.19 kDa, four times the theoretical monomer mass (19.43 kDa),

indicating that FlgX forms a tetramer in solution (Fig. 1C). In addition, circular dichroism (CD) spectrum of FlgX showed the characteristic 208 and 218 nm negative peaks (Fig. 1D), in agreement with the helical and β -sheet structure of tPilZ. Moreover, CD-based thermal denaturation assay revealed that the melting temperature of FlgX is 64 °C, suggesting a stable tetramer (Fig. 1E).

In the “house-like” structure of the tPilZ tetramer, four α 3 helices form the central pillars, with eight inclined α 2 and α 4 helices as the roof and four β -barrel folds as cornerstones (45). AlphaFold prediction of the FlgX tetramer suggested the same “house-like” architecture (Fig. 1B). As the C-terminal α 4 points outward from the roof, with residues 150 to 165 forming the roof eaves, we hypothesized that truncation of the eave fragment or fusion of another protein domain to the edge of the eave would not alter the tetramer core structure. As expected, SEC-MALS assays for the truncated FlgX construct (FlgX ^{Δ aa150-165}) and sfGFP fusion (FlgX-sfGFP) showed that both form tetramers in solution (Fig. 1C), providing additional evidence for the tetramer formation of FlgX.

In XCC6012, the hydrophobic residues in α 3 are critical for tetramer formation via strong hydrophobic heptarepeats, further strengthened by intermolecular salt bridges formed by the ⁷⁵DAKLD⁷⁹ motif in α 3 (45). This domain-interlocking motif was later generalized to [DENH]X[KR]h[DEN] based on sequence alignment of >3,000 tPilZ homologs (38). However, the corresponding position of this motif in FlgX is ⁶⁴KEDIL⁶⁸, which does not match the above amino acid residues of the generalized motif. This difference explains why FlgX was not recognized as a tPilZ protein in the comprehensive search in the NCBI protein database (38). To test whether the charged residues in ⁶⁴KEDIL⁶⁸ are crucial for stabilizing the FlgX tetramer, K⁶⁴ and D⁶⁶ were mutated to alanine, generating FlgX^{K64A}, FlgX^{D66A}, and FlgX^{K64AD66A}. SEC-MALS assays for these constructs showed that only substitution of K64 to alanine disassociates the FlgX tetramer to a dimer, while both FlgX^{D66A} and FlgX^{K64AD66A} remain tetramers (SI Appendix, Fig. S2). It is unclear why mutation of both K64 and D66 to alanine does not affect tetramer formation but mutation of K64 to alanine does. Nevertheless, as the proposed domain-interlocking motif [DENH]X[KR]h[DEN] is missing from the FlgX sequence, this motif should be redefined or removed as a criterion for inclusion in the tPilZ protein family.

Given the high confidence score of the structure prediction, tPilZ characteristics, and stable tetramer formation, FlgX likely belongs to the tPilZ family, a notion that can be verified in future by obtaining the X-ray structure.

FlgX Does Not Bind c-di-GMP, and aa¹⁵⁰⁻¹⁶⁰ in α 4 Play an Important Role in FlgX Function. The FlgX sequence lacks the RXXXR and [D/N]hSXXG motifs essential for binding of c-di-GMP in PilZ superfamily proteins (Fig. 1A) (38, 39). To verify c-di-GMP binding, isothermal titration calorimetry (ITC) was performed for full-length wild-type FlgX. PA2989 from *P. aeruginosa*, a tPilZ family protein with the c-di-GMP binding motif, binds c-di-GMP (46). Thus, PA2989 was selected as a positive control for ITC assay and binds c-di-GMP at a K_D of 188 nM (Fig. 2A). By contrast, no reliable binding of c-di-GMP was obtained for FlgX (Fig. 2A). In addition, our prior comparative genomic studies showed that the genomes of subgroup II of the genus *Campylobacter*, which includes the species *C. jejuni*, do not encode an active GGDEF domain-containing protein that can synthesize c-di-GMP (47). Among 267 analyzed *C. jejuni* genomes, only two genes that encode the GGDEF domain were identified per genome, corresponding to proteins CbrR (Dgc_03) and VidB (Dgc_01) (47). These two proteins from *C. jejuni* 81-176

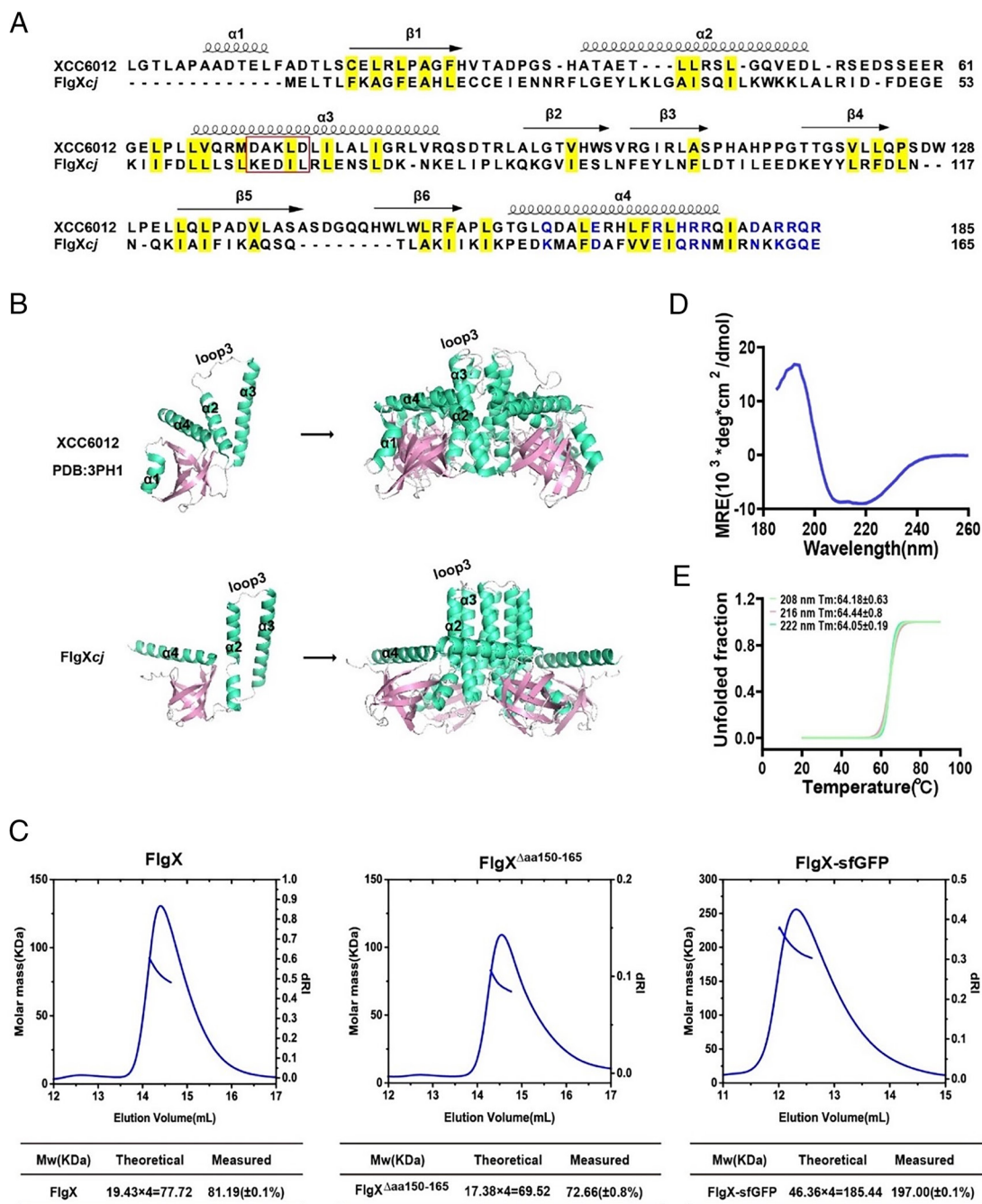


Fig. 1. FlgX belongs to the tPilZ protein family. (A) A structure-guided sequence alignment of FlgXcj and XCC6012. The secondary structure elements (β-strand [arrow] and α-helix [curly]) are from XCC6012 structure (PDB entry: 3PH1). Conserved hydrophobic residues are shaded in yellow, and C-terminal charge residues are colored in blue. (B) AlphaFold prediction of FlgXcj structure and comparison with XCC6012 structure. The structures are colored by secondary structure. The overall confidence value is over 80 for FlgXcj monomer and tetramer. (C) SEC-MALS results for the oligomerization status of FlgX and its variants either truncated at the C-terminus or fused with sfGFP. The measured molecular weights are expressed as Mw (±%) and recorded in table below each graph. (D) CD spectra analyses of FlgXcj at 185 to 260 nm. (E) CD-based thermal denaturation assay of FlgXcj.

lack enzymatic activity for c-di-GMP production (48). Hence, FlgX in *C. jejuni* is not regulated by c-di-GMP as the protein itself lacks the binding motif, and its host species does not produce this secondary messenger.

Another link between FlgX and tPilZ or canonical PilZ domains exists in their C-terminal helix, which is enriched by charged amino acid residues, particularly Arg and Lys (Fig. 1A) (38, 39). In addition, as all the other structural elements are critical for tetramer formation (α2 and α3) or the core β-barrel fold (β1-β6), the C-terminal helix region may mediate interaction with other proteins, as in the case of MapZ and YcgR (42, 43). To explore the structural and functional role of the α4 helix in FlgX, several

truncation mutants were generated. The truncated variants of the α4 helix at different lengths for *flgX* were introduced into the *ΔflgX* mutant, and the generated mutants were tested for motility on soft agar. Meanwhile, the truncated variants were expressed and purified from *E. coli* for oligomerization assays. Only complementation of full-length FlgX and FlgX lacking the last 5 amino acids restored the motility of the *ΔflgX* mutant to wild-type levels, while all other FlgX variants failed (Fig. 2B). Truncation of the entire α4 helix (residues 140 to 165) or most of it (residues 145 to 165) likely destabilized the FlgX tetramer because overexpression of these two constructs in *E. coli* yielded inclusion bodies. By contrast, the other three truncation constructs, FlgX^{Δa150-165}, FlgX^{Δa155-165},

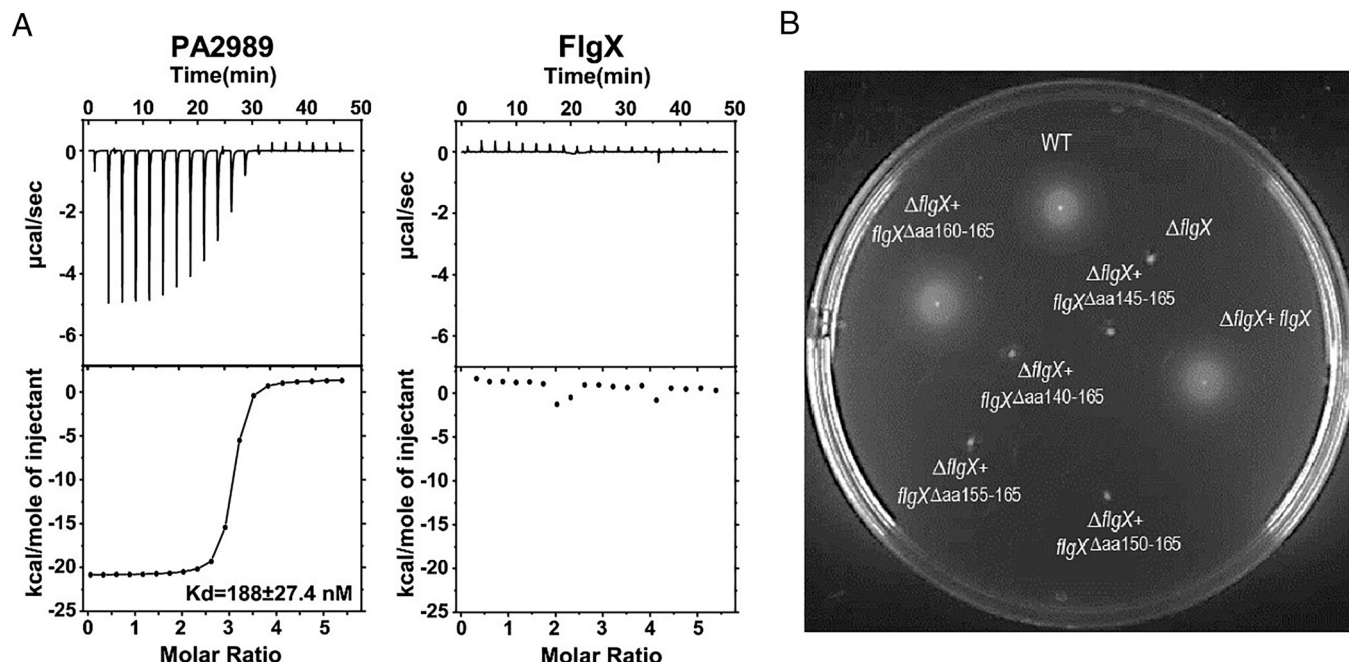


Fig. 2. FlgX does not bind c-di-GMP, and aa¹⁵⁰⁻¹⁶⁰ in $\alpha 4$ is functionally important. (A) ITC results of positive control PA2989 and FlgX_{cj}. The *Top* trace shows raw titration data collected at 25 °C in binding buffer (10 mM Tris-Cl, pH 8.0, 150 mM NaCl), while the *Bottom* trace shows dilution heat-corrected and concentration-normalized integrated peak areas of raw data. Titration of c-di-GMP into the PA2989 solution yielded a K_d of 188 ± 27.4 nM using a one-site binding model. No binding trend was detected for FlgX. (B) Soft agar motility assay of $\Delta flgX$ mutant and complementation with various truncated flgX variants.

and FlgX ^{Δ aa160-165}, are all easily overexpressed and purified and form tetramers in solution (Fig. 1C and *SI Appendix*, Fig. S3). Overall, residues 150 to 160 in $\alpha 4$ helix are important for FlgX function but not involved in tetramer formation.

FlgX Is Required for Assembly of the Stator Ring and Formation of the Intact FliL Rings. As FlgX can repeatedly coimmunoprecipitate with both MotA and MotB from *C. jejuni* cell lysate (36, 37), and without data on the subcellular localization of FlgX in the cytoplasm, we hypothesized that FlgX is a structural component, rather than chaperone, in the *C. jejuni* motor. We examined the motor structures of wild-type *C. jejuni* and the $\Delta flgX$ mutant using cryo-ET and subtomogram averaging (Fig. 3). Cryo-EM images of the whole cells showed one flagellum at each pole in both wild type and the $\Delta flgX$ mutant (*SI Appendix*, Fig. S4). Cryo-ET imaging of the cell poles revealed flagellar motor structures including motor components both in periplasmic and cytoplasmic regions (*SI Appendix*, Fig. S4), supporting the prior finding that FlgX is not essential for flagellar assembly in *C. jejuni* (36).

To understand the differences between wild type and the $\Delta flgX$ mutant, we determined their motor structures using cryo-ET and subtomogram averaging, respectively (Fig. 3 A–J). Our in situ structure of wild-type flagellar motors revealed features consistent with previous reports (23, 49), including the periplasmic basal/medial/proximal disks, 17 FliL rings, 17 stator complexes, and C-ring (Fig. 3 A–E). Importantly, we also observed extra densities underneath each of the stator complexes in cytoplasmic space (Fig. 3 D and E). The extra densities had not been previously reported in *C. jejuni* or other bacterial species (Fig. 3 D and E). By contrast, both the stator complexes and extra densities are absent from our in situ $\Delta flgX$ motor structure, while all other motor structures resemble those of the wild-type motor, except some noticeable changes in the FliL rings and cage structure discussed in detail later (Fig. 3 F–J and *SI Appendix*, Fig. S5). The absence of the stator complexes from the $\Delta flgX$ motor provides structural evidence for the prior finding that the stability of stator

proteins (MotA and MotB) is dependent on FlgX (37), though does not clarify whether FlgX is a chaperone or structural component constituting the extra densities beneath the stator units.

To better define the stator units and their impact on motor structure, we used cryo-ET and subtomogram averaging to determine the motor structure of a *C. jejuni* $\Delta motA$ mutant (Fig. 3 K–O and *SI Appendix*, Fig. S4). The motor structures from $\Delta motA$ and $\Delta flgX$ are identical, and neither the stator units nor the densities underneath the stator units are visible (Fig. 3 F–O), suggesting that the extra densities underneath the stator units are dependent on the presence of both MotA and FlgX, in addition to the dependence of stator ring assembly on FlgX.

The FlgX Tetramer Fits the Half Rings Underneath MotA. To gain more detail for the extra densities below the stator units, focused refinement was performed for the stator complex and its surrounding motor components in the wild-type flagellar motor (Fig. 4 A–C). The stator complex, including MotA and MotB subunits (4, 5), is well resolved in the refined map (Fig. 4 B–D). Intriguingly, the in situ structure reveals that the peptidoglycan (PG) layer binding domain of the MotB complex (23, 50–52) is tilted slightly inward and the N-terminal domain adopts a bent conformation to insert into the MotA ring (4, 53, 54) (Fig. 4 B and C). Furthermore, the N-terminal domain is also surrounded by a FliL ring. Unlike in *B. burgdorferi* and *H. pylori* (31, 32), the FliL ring appears asymmetric and tilted along the inner membrane in *C. jejuni* (Fig. 4 B and C).

On the cytoplasmic side of the stator complex, our refined structure clearly reveals two half-ring structures underneath the pentameric structures of MotA (Fig. 4 D and E). The inner half ring located near the C-ring appears stronger than the outer half ring, suggesting that the inner half ring near the C-ring is relatively stable compared to the outer half ring (Fig. 4E). Finally, a globular density (Figs. 3E and 4F), here termed connector, appears to bridge two adjacent half rings between two stator units (Fig. 4 F and G).

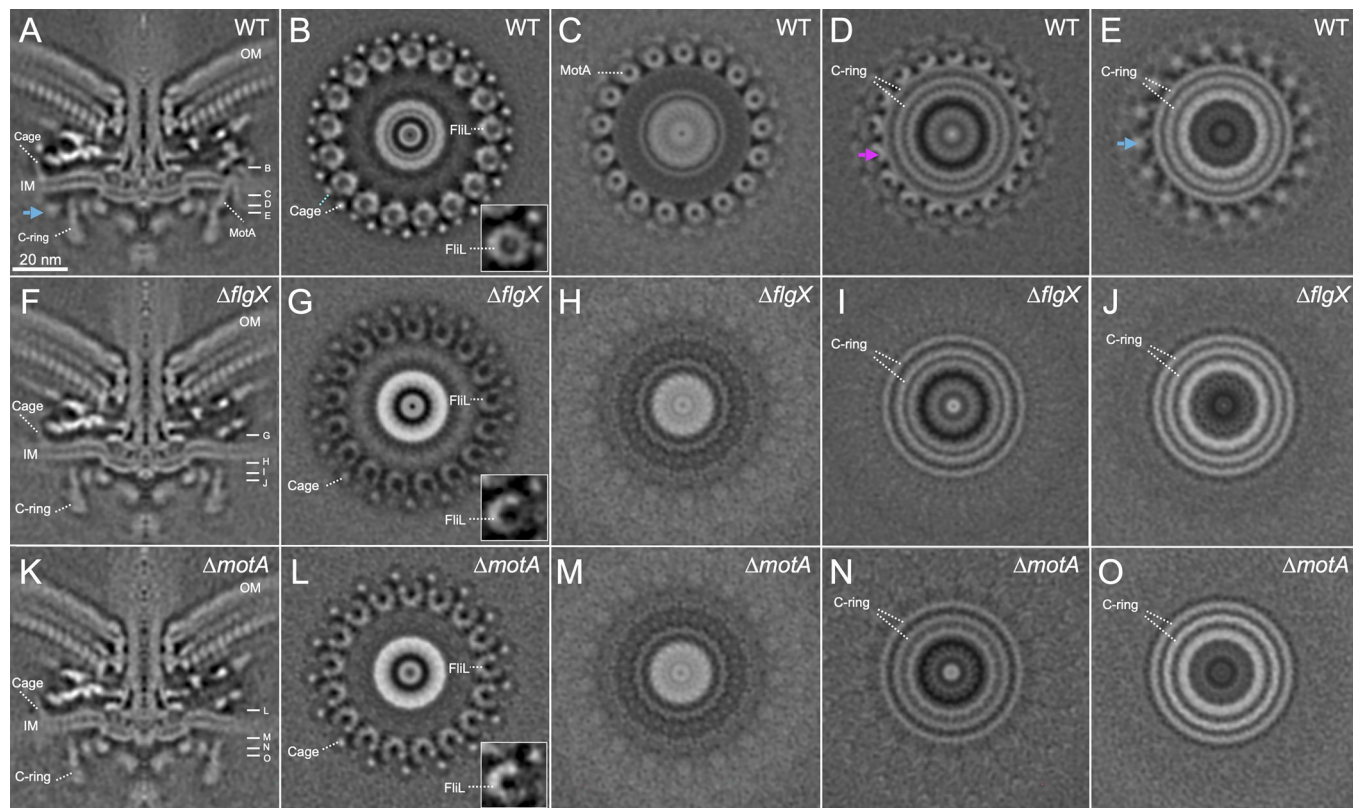


Fig. 3. In situ structures of the flagellar motors in *C. jejuni* wild type, $\Delta flgX$, and $\Delta motA$. (A) A central section of the in situ motor structure in wild type shows major flagellar components including stator units and C-ring as well as the OM and IM. Four different cross sections of the periplasmic (B) and cytoplasmic (C) stator regions and two regions underneath (D) and (E). There are 17 FilL rings and 34 cage subunits in the wild-type motor (B). The *Inset* is a focused refined structure of the FilL ring adjacent to two cage subunits (B). There are 17 MotA rings (C). Half-ring densities under MotA are indicated with a magenta arrow in panel (D) and other globular densities under the half-ring structure are indicated with a blue arrow in panels (A) and (E). (F) A central section of the in situ structure of the $\Delta flgX$ flagellar motor is almost identical to that of the flagellar motor in wildtype (A), except for the stator units, cage, and globular densities. (G) Cross-section of the periplasmic region shows 17 incomplete FilL rings and 17 cage subunits. The *Inset* is a focused refined structure of the incomplete FilL ring. (H–J) Three cross sections of the cytoplasmic region of the $\Delta flgX$ flagellar motor show features different from the corresponding sections in the wild-type motor (C–E). (K) A central section of the in situ structure of the $\Delta motA$ flagellar motor is identical to that of the $\Delta flgX$ flagellar motor. (L) Cross-section of the periplasmic region shows 17 incomplete FilL rings and 17 cage subunits. The *Inset* is a focused refined structure of the incomplete FilL ring, which is adjacent to one cage subunit. (M–O) Three cross sections of the cytoplasmic region of the $\Delta motA$ flagellar motor show features similar to those in the $\Delta flgX$ flagellar motor (H–J).

As FlgX localizes exclusively to the *C. jejuni* cytoplasm and likely directly interacts with MotA (37), it is possible that FlgX constitutes the two half-ring densities under the MotA pentamer (Fig. 4 G and H). To verify the location of FlgX, we introduced sfGFP fusions at its N- or C-terminus, with and without the linker sequence of different lengths, into the $\Delta flgX$ mutant. However, none of these sfGFP fusions restored motility, suggesting an alteration of FlgX function due to the fusion and thus making the constructs unsuitable for cryo-ET imaging (SI Appendix, Fig. S6). These FlgX constructs with sfGFP fusion were also overexpressed and purified from *E. coli* for SEC-MALS oligomerization assays, and all formed tetramers in solution (Fig. 1 C and SI Appendix, Fig. S2). Collectively, these results indicate that sfGFP addition does not alter the FlgX core structure but does affect FlgX function in *C. jejuni*, possibly jeopardizing its interaction with stator complexes.

Alternatively, the predicted structure of the MotA₅FlgX₄ complex based on AlphaFold3 (SI Appendix, Fig. S7) shows that $\alpha 2$ and $\alpha 3$ in FlgX, which are involved in the tetrameric formation as well as essential for motility (Fig. 2B), insert into the MotA pentamer. To test the predicted structure, we docked it into the refined cryo-ET structure (Fig. 4H). Both the stator complex and FilL-ring fit well into the map. However, the predicted FlgX tetramer does not fit into the two half-ring densities underneath the MotA pentamer as the distance between the two half rings is 7.8 nm which is longer than 5.0 nm seen in the predicted FlgX tetramer model (SI Appendix, Fig. S7). We decided to remodel the FlgX tetramer

as two dimers, each of them could fit well into the half-ring densities as a rigid body, respectively (Fig. 4I) (SI Appendix, Fig. S7). Though we cannot rule out other possible models, our data strongly suggest that two FlgX dimers are located under the stator unit and form the complex with MotA. Additional unknown proteins are likely involved in formation of the connector bridging two adjacent FlgX tetramers underneath stator complexes (Fig. 4I).

To further verify that FlgX constitutes the half-ring densities underneath MotA pentamer, we performed point mutagenesis on both FlgX and MotA based on our model of the MotA₅FlgX₄ complex (Fig. 4 I and J). Multiple residues in $\alpha 2$ and $\alpha 4$ of FlgX and the cytoplasmic region of MotA were predicted to be involved in the interaction of these two proteins (SI Appendix, Fig. S8). For MotA, some residues are universally conserved in various species across bacterial phyla and have been experimentally validated as important for its structure or function in the model organism *S. enterica* (4). Thus, the above residues in MotA were not selected, while the following residues were chosen for point mutation: L⁹³, L⁹⁴, and V¹¹⁶ of MotA that were predicted to interact with Q¹⁵⁴ and I¹⁵⁸ in $\alpha 4$ of FlgX; R¹⁵⁵ and R¹⁵⁹ in $\alpha 4$ of FlgX; and E¹²², H¹²⁵, and E¹²⁹ of MotA that were predicted to interact with K⁴² and R⁴⁶ in $\alpha 2$ of FlgX (Fig. 4 J and K and SI Appendix, Fig. S8). Soft agar motility assays for these mutants showed that mutation of L⁹³ or V¹¹⁶ in MotA severely impaired motility and that these residues are involved in interaction with FlgX- $\alpha 4$ (SI Appendix, Fig. S8). By contrast, mutation of E¹²², H¹²⁵, and E¹²⁹ of MotA that were predicted to interact with FlgX- $\alpha 2$ did

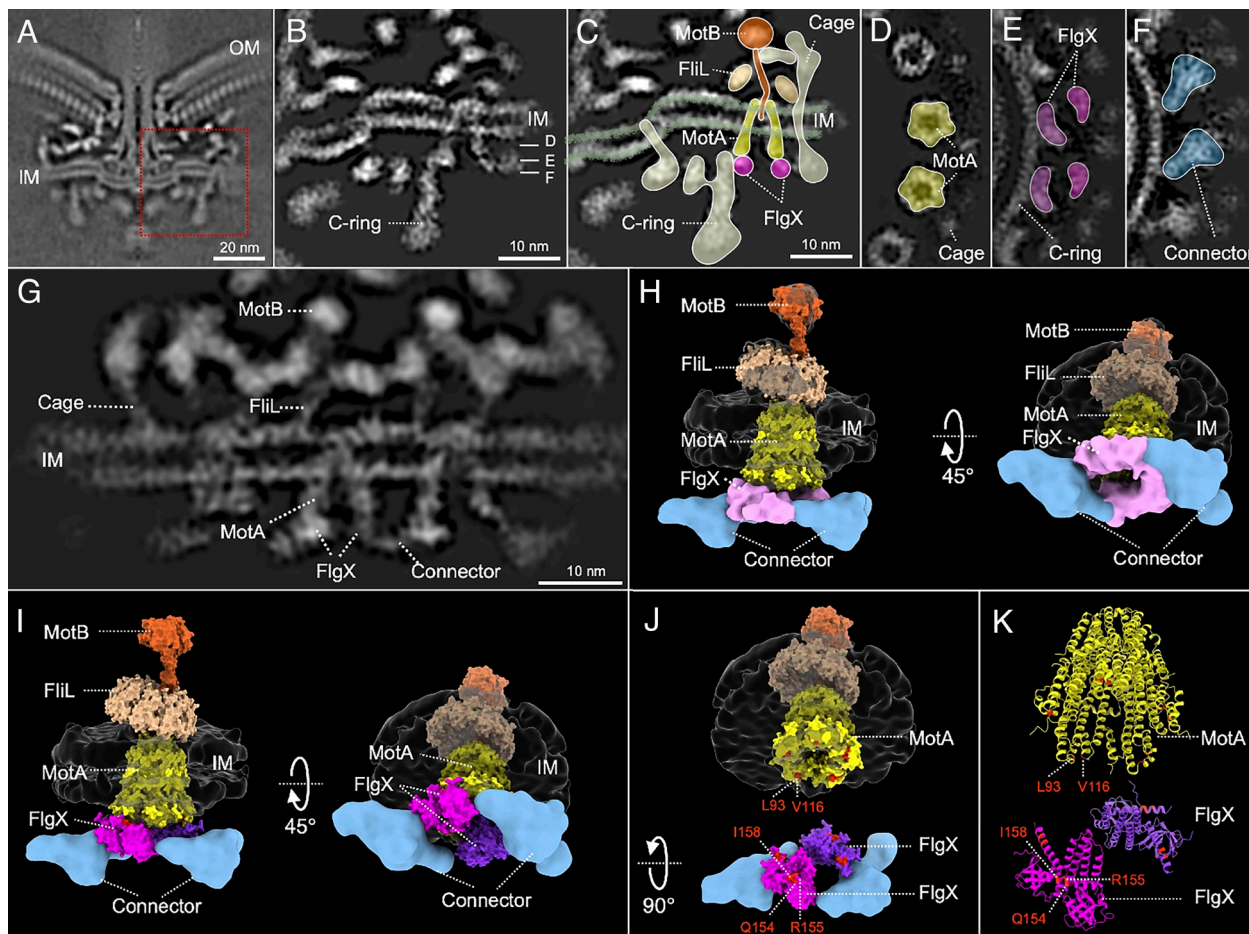


Fig. 4. The refined in situ structure reveals a distorted ring underneath the MotA pentamer. (A) The central section of the complete *C. jejuni* flagellar motor structure. The inner membrane complex indicated in the red square was refined to analyze structural details. The refined structure (B) and its cartoon model (C) show that MotB has a bent coiled-coil structure (orange), asymmetric FliL ring (light brown), MotA ring (yellow), and two half rings of FlgX (magenta) underneath MotA, as well as other motor components. Three different cross sections show the MotA pentamer (D), two half rings underneath the MotA pentamer (E), and globular densities under the half rings (blue) (F). (G) The vertical cross-section of the MotA pentamer with the proximal disk component showing MotA, the half rings, and the globular densities that connect each pair of the half ring. (H) Fitting of the predicted structures of MotA, MotB (32), and FliL into the in situ structure shows the extra densities underneath the MotA pentamer. (I) Each FlgX dimer in the predicted tetramer fits well into the half ring structures (magenta and purple). (J) A 90° tilt of FlgX from the stator complex shows the interface of the FlgX–MotA complex. (K) The zoom-in view of the interface between MotA and FlgX shows residues (colored in red) critical for the complex formation.

not significantly alter motility. In addition, mutations of single residue Q¹⁵⁴, R¹⁵⁵, or I¹⁵⁸ in $\alpha 4$ of FlgX to alanine either severely or moderately impaired motility, while all mutations in residues of FlgX- $\alpha 2$ did not show an effect on motility (SI Appendix, Fig. S8). Moreover, double mutation of R¹⁵⁵ and R¹⁵⁹ in $\alpha 4$ of FlgX completely abolished motility, suggesting that charged residues in C-terminal $\alpha 4$ play an important role in FlgX function (SI Appendix, Fig. S8). Taken together, the point mutagenesis results support that FlgX- $\alpha 4$ interacts with the loop regions of the MotA pentamer predicted by AlphaFold3 but do not support that FlgX- $\alpha 2$ inserts into the bottom cavity of the MotA pentamer (Fig. 4J and SI Appendix, Fig. S8), consistent with the confidence level of the predicted complex structure (SI Appendix, Fig. S7). Last, our modification of the orientation of the FlgX tetramer based on the densities from the two half rings also showed that the cavity of the MotA pentamer is not occupied by the FlgX tetramer (Fig. 4I and SI Appendix, Fig. S7).

The FlgX–Stator Complex Is Required for the Formation of Intact FliL Rings as Well as Intact Cage. While the flagellar motor structure from Δ flgX lacks stator units, the periplasmic basal/medial disks and C-ring that surround or interact with stator complexes remain intact (Fig. 3A–F). Notably, the FliL structures in the Δ flgX and Δ motA mutants differ from those in wild type

(Fig. 3B, G, and L). FliL in wild-type *C. jejuni*, *B. burgdorferi*, and *H. pylori* forms ring structures (Fig. 3B) (31, 32). By contrast, FliL in both *C. jejuni* Δ flgX and Δ motA mutants forms a partial, “U”-shaped ring (Fig. 3G and L), similar to but bigger than the partial FliL ring in the Δ motB mutant of *B. burgdorferi* (32). The presence of the incomplete FliL ring in the *C. jejuni* Δ flgX mutant supports sequential assembly of the FliL–stator complex, whereby FliL oligomerizes from a partial into a full ring (31). In addition, 34 copies of cage structures are present in wild type (Fig. 3B), whereas the Δ flgX and Δ motA mutants contain 17 copies due to the absence of a cage near “U”-shaped FliL (Fig. 3G and L). The latter phenotype suggests that the cage near the FliL ring assembles after stator association, possibly enclosing the stator units within the motor. Hence, the presence of FlgX, the full FliL ring, and 34 copies of cage structures enable *C. jejuni* to load 17 stator units in generating high rotational torque required for motility (Fig. 5).

FlgX Likely Evolved in the Common Ancestor of Campylobacterota. FlgX homologs exist in many but not all species of the Campylobacterota phylum. Despite the conserved protein fold, the low sequence similarity of FlgX homologs, which is a characteristic of the tPilZ family, makes it difficult to identify tPilZ proteins by homology alone (SI Appendix, Fig. S9) (38). Interestingly, the

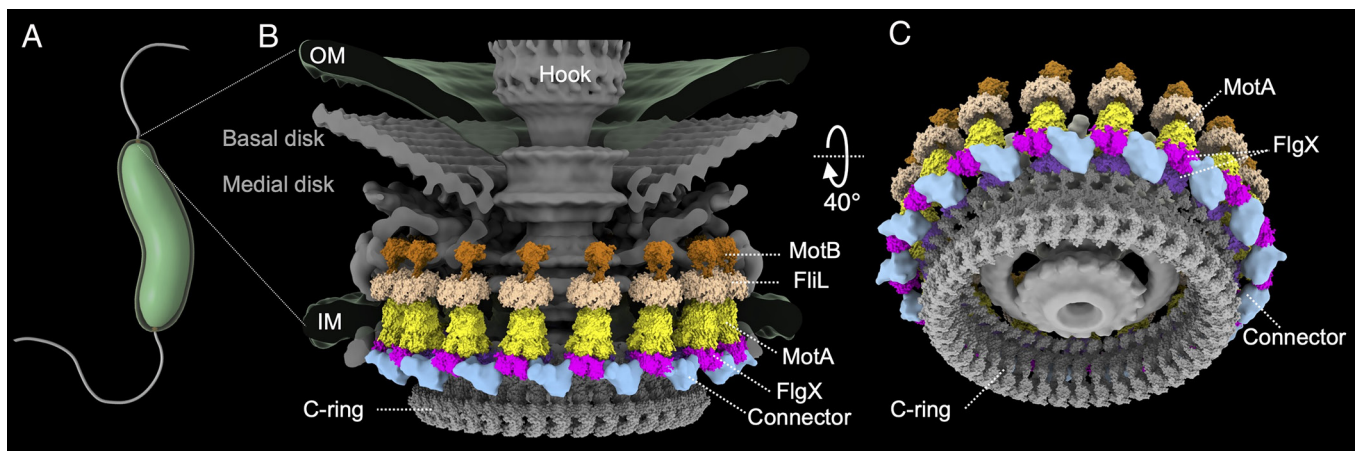


Fig. 5. Pseudoatomic model of the FlgX–MotA complex in the *C. jejuni* flagellar motor. (A) An overview of an intact *C. jejuni* cell with two polar flagella. (B) A side view of the intact *C. jejuni* flagellar motor highlights the interface between the stator complex and FlgX. To show the interactions clearly, the front side of the OM, IM, and periplasmic components are removed. (C) A tilted view of the motor shows the cytoplasmic components, including MotA pentamers, FlgX tetramers, and the unknown connectors adjacent to the C-ring.

order of genes neighboring *flgX* is conserved in *Campylobacterota* species, with *ubiA* upstream and *flgW* downstream (Fig. 6). This conserved gene order enabled the identification of *flgX* homologs in this phylum by searching for the conserved *ubiA* gene first, then using HHpred or AlphaFold to predict the downstream protein sequence. Finally, FlgX homologs were identified with confidence in 72% species of the *Campylobacterota* phylum but missing from the genera *Nitratiruptor*, *Nitratifactor*, *Sulfurovum*, and *Arcobacter* and from a few species of the genus *Campylobacter* (Fig. 6 and SI Appendix, Table S1).

To understand the evolution of FlgX in *Campylobacterota*, its homologs were mapped in a species tree showing the flagellation status and chemosensory class collected from our recent studies (Fig. 6) (55). The absence of an FlgX homolog from the genera *Nitratifactor* and *Sulfurovum* and a few *Campylobacter* species is clearly due to loss of flagella (Fig. 6). In addition, the genera *Nitratiruptor* and *Arcobacter*, which lack FlgX homologs but are flagellated, belong to a chemosensory class other than the F3 class unique to the phylum (Fig. 6) (55, 56). By contrast, all *Campylobacterota* species with FlgX homologs have the F3 class (Fig. 6).

Our recent phylogenomic studies on the coevolution of the chemosensory system and flagella in *Campylobacterota* suggested that species with the F3 class obtained their flagellar gene set from the last common ancestor of the phylum (55). By contrast, the genera *Nitratiruptor* and *Arcobacter* switched F class due to loss of ancestral flagellar genes or massive genome-wide rearrangement of flagellar genes (55). Hence, the co-occurrence of FlgX homologs with both the F3 class and ancestral flagellar gene set suggests that FlgX was already present in the last common ancestor of this phylum (Fig. 6). In addition, loss or massive alteration of the ancestral flagellar gene set among species of this phylum led to loss of FlgX.

To test the functional conservation of FlgX in *Campylobacterota*, FlgX homologs from three species were chosen for biochemical characterization, including host-associated *Helicobacter typhlonius*, deep-sea hydrothermal vent-isolated *Hydrogenimonas thermophila*, and *Caminibacter mediatlanticus*. SEC-MALS assays showed all three proteins form tetramers in solution (SI Appendix, Fig. S10). ITC experiments also suggest that they do not bind c-di-GMP, consistent with all FlgX homologs in *Campylobacterota* lacking the motif for c-di-GMP binding (SI Appendix, Figs. S9 and S10). Given the conserved gene order of *flgX* with downstream flagellar gene *flgW* and the co-occurrence of FlgX homologs with both the F3 chemosensory class and the ancestral flagellar gene set, the FlgX homolog likely also associates with stators in each *Campylobacterota*

species and represents an ancient adaptation that arose when the ancestor of this phylum emerged.

Discussion

The structure of the PilZ domain is an ancient protein fold, based on its ubiquity in *Bacteria* as well as divergence in structure (PilZ, tPilZ, xPilZ) and function (38). Previous studies on PilZ domain-containing proteins revealed only their role as receptors for c-di-GMP. All subsequent physiological changes were caused by c-di-GMP binding, which promoted interaction between these receptors and other proteins. Here, our studies reveal a role for tPilZ as a stable structural component in the flagellar motor, independent of c-di-GMP regulation. Hence, the PilZ domain has been adopted by nature for various purposes.

Though all are members of the PilZ superfamily, FlgX differs from other PilZ domain-containing proteins engaged in motor regulation, such as YcgR/MotI. Both YcgR and MotI dynamically interact with the motor and inhibit motility in various bacterial species (34, 35, 42). By contrast, FlgX is a stable motor component and is essential for motility in *C. jejuni*. Moreover, FlgX is the sole PilZ superfamily protein in *C. jejuni*, which has no YcgR or MotI homolog. As suggested by earlier bioinformatic analyses, many bacterial genomes encode multiple PilZ domain-containing proteins with different domain organizations yet unknown functions (38, 39). Prior studies and ours have only begun to reveal the versatility of the PilZ superfamily.

Our findings also further elucidate the function of the stator unit. In *C. jejuni*, *H. pylori*, and *B. burgdorferi*, periplasmic scaffolds play an important role in assembly and function of the stator ring (23, 24, 30). Our cryo-ET structure shows that the PG binding domain of MotB is pushed inward slightly by other periplasmic components and that the helix region of MotB has a bent conformation allowing it to pass through the FliL and MotA rings. In a general model, interactions of this domain with the PG layer are essential for MotB to adopt its extended conformation for stator units to generate rotational torque. As the PG layer is absent from our in situ structures, other motor components in the proximal disk likely maintain MotB in this active conformation. These additional periplasmic structures surrounding the central rod may also enable more stator units to be incorporated into the motor, thus generating sufficient torque for faster swimming.

FlgX interacts with the bottom part of the stator units in the cytoplasm, and no cytoplasmic scaffold has been reported for the

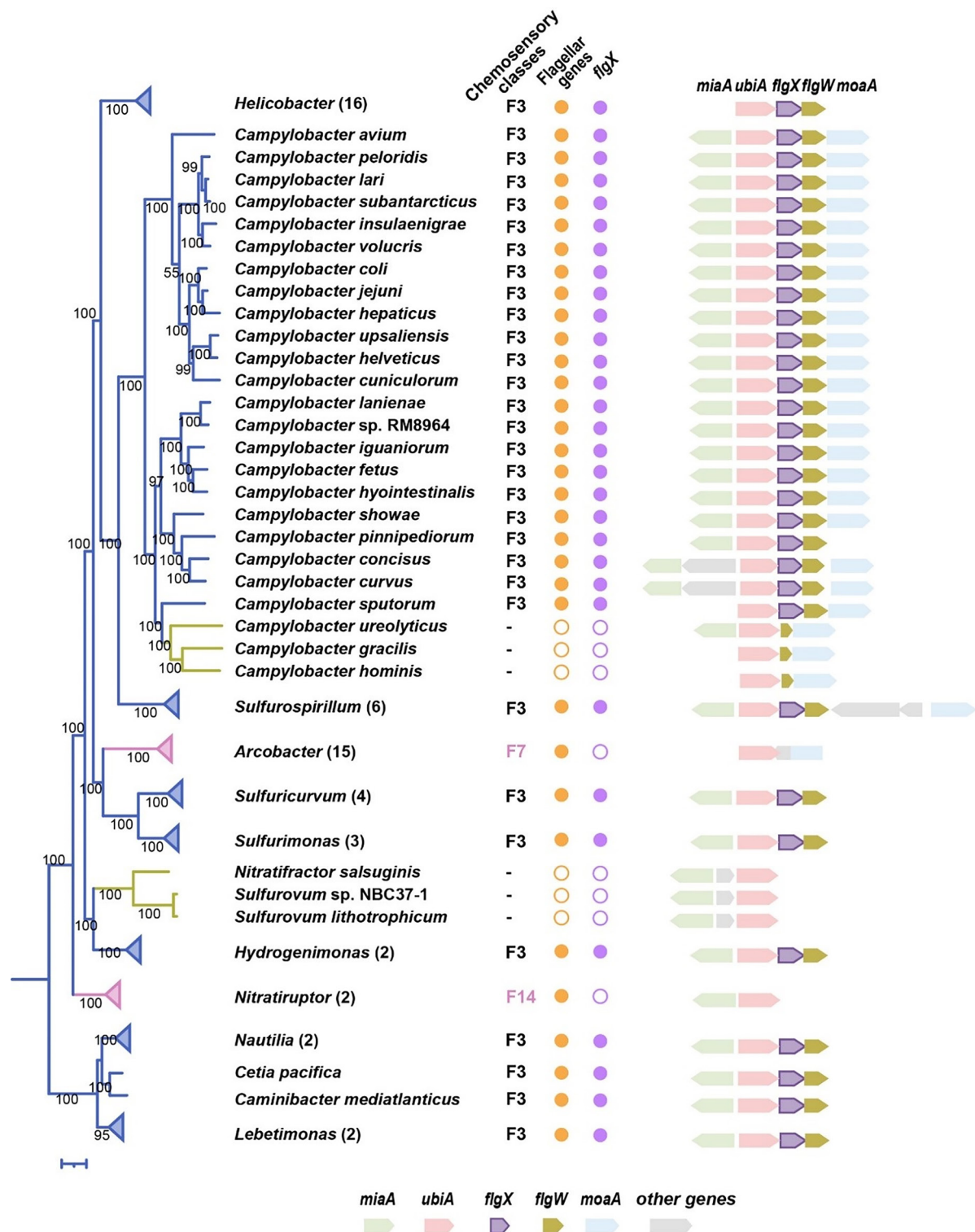


Fig. 6. FlgX homologs, conserved gene order, and coevolution with F3 chemosensory class in the phylum *Campylobacterota*. The phylogenetic tree of representative species of *Campylobacterota* was taken from *SI Appendix, Fig. S1* of ref. 36. The triangles in the tree represent collapsed branches for multiple species that belong to the same genus and have the same F class controlling flagellar motility. The numbers in brackets on the right of some genera indicate the number of species analyzed.

flagellar motor (Fig. 5). The in situ structure and FlgX model suggest that two FlgX tetramers interact with the connector, acting as a new cytoplasmic scaffold for stator units (Fig. 5). It would therefore be intriguing to examine whether FlgX rotates with the stator or remains fixed in the cytoplasm. Moreover, the cytoplasmic region of MotA interacts with the “torque helix” of FliG (57), and recent structural studies have revealed mechanistic details

underlying how the stator units and C-ring change their relative position during a switch in rotational direction (17, 18, 20, 21). It will be worthwhile to explore in future how FlgX fits into this interplay and affects torque generation.

Finally, as FlgX is a member of the tPilZ family, the origin of its protein fold is well understood, but the evolution of FlgX/tPilZ in the *Bacteria* domain remains unclear. It has been proposed that

insertion of a ~200 bp fragment of tPilZ, corresponding to the ~60-aa insert of the α -2 and α -3 helices, into canonical PilZ results in formation of tPilZ (38). Based on the close association of many PilZ family proteins, such as YcgR/MotI, with the flagellar motor, it is tempting to ask whether tPilZ was an original component or later neofunctionalized in an ancestor of *Campylobacterota*. In addition, tPilZ domains generally adopt a stand-alone form with encoding genes in a single copy per genome, quite different from other PilZ domains with various domain combinations and multiple copies (38). To establish association of tPilZ with the flagellar motor, particularly with the 5:2 rotary stator, it will be important to investigate the function of tPilZ proteins (or FlgX homologs) across bacterial phyla.

Materials and Methods

Bacterial Strains and Culture Conditions. The strains, plasmids, primers, and relevant antibiotics are detailed in *SI Appendix, Tables S2 and S3*. *C. jejuni* 81 - 176 wild-type and mutant strains were cultured on blood agar plates at 37 °C in a BACTROX-2 microaerobic workstation (SHELLAB, USA) set to 5% O₂ and 10% CO₂. Liquid cultures of *C. jejuni* were grown in BHI medium, and mutants were selected on *Brucella* Bruth agar plates supplemented with specified antibiotics (*SI Appendix, Table S2*). *E. coli* was cultured on LB medium or agar plates at 37 °C aerobically. Antibiotics were added to the selection medium at the following concentrations: chloramphenicol (50 µg/mL for *E. coli*, 10 µg/mL for *C. jejuni*), kanamycin (50 µg/mL), apramycin (50 µg/mL), and ampicillin (100 µg/mL). *C. jejuni* strains were stored at –80 °C in BHI medium with 30% glycerol, and *E. coli* strains were stored at –80 °C in LB medium with 15% glycerol.

***C. jejuni* Mutant Construction and Complementation.** *C. jejuni* 81 - 176 knockout mutants were generated using a gene insertion or replacement approach. This involved inserting an antibiotic resistance cassette into the target gene's open reading frame according to established methods (58). Upstream and downstream regions of the target gene (approximately 800 bp each) were PCR amplified, with BamHI or EcoRI restriction enzyme cutting sites introduced in the middle. These fragments were then fused into the linearized pBluescript II SK plasmid using the Gibson assembly protocol (59). After digestion with BamHI or EcoRI enzymes, a kanamycin gene cassette was inserted using T4 ligase. The resulting recombination plasmids were transformed into *E. coli* DH5 α , and transformants were selected on LB plates containing kanamycin. Plasmids were verified by DNA sequencing before being naturally transformed into *C. jejuni* 81 - 176 for gene allelic exchange. Transformants were selected on *Brucella* broth agar plates supplemented with kanamycin, and mutations were confirmed by PCR analysis and DNA sequencing.

The *C. jejuni* gene knockout mutants were complemented by inserting the wild-type copy of the target gene into the *hdsR* locus. This was achieved by incorporating a chloramphenicol resistance cassette and a 3XFLAG tag fused to the target gene, following established protocols (58). Complemented mutants were selected on *Brucella* broth agar plates containing chloramphenicol and kanamycin. PCR tests were conducted to confirm the recombinant gene regions in all constructs.

De Novo Modeling and Structural Alignment. The full-length structure of FlgX was generated using ColabFold, an online implementation of AlphaFold2 (60, 61). The structure of XCC6012 was retrieved from the PDB database. Next, Discovery Studio (<https://www.3ds.com/products/biovia/discovery-studio/visualization>) was used to align the two three-dimensional structures by minimizing the overall RMSD. Based on the results of the structural alignment, the structural information was converted into sequence alignment, producing a sequence alignment result that includes structural information. Finally, alignments were supplemented with those generated by the HHpred tool from the MPI Bioinformatics toolkit (62).

Protein Expression and Purification. The coding regions of *C. jejuni* FlgX (Accession No.: WP_002854663.1) were PCR amplified and ligated into the pET28a expression vector using Gibson assembly. Sequences of FlgX homologs from *H. typhlonius* (Accession No.: WP_034326073.1), *C. mediatlanticus* (Accession No.: WP_007475007.1), and *H. thermophila* (Accession No.: WP_092912120.1) were obtained from NCBI GenBank and synthesized by

Sangon Biotech (China). Codon optimization was performed on the DNA fragment encoding FlgX from *C. mediatlanticus* and *H. thermophila* to ensure normal protein expression.

All proteins were overexpressed in *E. coli* BL21 (DE3) cultured in 1 L Erlenmeyer flasks containing 600 mL LB medium supplemented with 50 µg/mL kanamycin at 37 °C until reaching an OD₆₀₀ of 0.6 to 0.8. Induction of protein production was initiated by adding 0.5 mM IPTG, followed by continued growth at 16 °C for 16 to 18 h. Cells were harvested by centrifugation at 5,000 g for 8 min, then resuspended in buffer A (20 mM Tris-HCl, 150 mM NaCl, 10 mM imidazole, pH 7.4) and lysed using JN-Mini ultra-high-pressure continuous flow cell disrupters (JNBIO, China). After centrifugation at 12,000 g for 30 min, the supernatant was loaded onto a gravity column containing 1.5 mL Ni-NTA Agarose (Qiagen, Germany). The column was washed successively with five column volumes of buffer A and buffer B (20 mM Tris-HCl, 150 mM NaCl, 50 mM imidazole, pH 7.4), and then eluted with 3 mL buffer C (20 mM Tris-HCl, 150 mM NaCl, 250 mM imidazole, pH 7.4).

SEC-MALS. Protein samples (typically 100 µL at a concentration of 500 µM, pre-equilibrated with column buffer) were injected into an ÄKTA FPLC system with a Superdex®200 Increase 10/300 GL column (Cytiva), using a buffer consisting of 20 mM Tris-HCl, 1 mM DTT, and 100 mM NaCl at pH 7.4. This chromatography setup was coupled to a multiangle light scattering system equipped with a 3-angle static light scattering detector (miniDawn, Wyatt) and a differential refractive index detector (Optilab, Wyatt). Elution profiles were analyzed using ASTRA 7 software (Wyatt).

Circular Dichroism Spectroscopy. CD spectra of FlgX (0.2 mg/mL) were recorded in a buffer containing 1 mM Na₂HPO₄ and 0.2 mM KH₂PO₄ at pH 7.4 using a Chirascan CD Spectrometer (Applied Photophysics) at 25 °C with a 1 mm path length cell. Each spectrum comprised three scans across a wavelength range of 185 to 260 nm. Thermal denaturation experiments were conducted on the same instrument, ramping the temperature from 20 to 90 °C in 1 °C increments with a dwell time of 1 min. Ellipticities at 208 nm, 216 nm, and 222 nm were utilized to determine the unfolded fraction plotted against temperature.

Isothermal Titration Calorimetry. ITC measurements were conducted at 25 °C using a MicroCal PEAQ-ITC instrument (MicroCal Inc.). Protein samples were dialyzed into a buffer containing 10 mM Tris (pH 8.0) and 150 mM NaCl. C-di-GMP (1 mM) was injected into a cell containing 35 µM protein using a sample syringe with a stirring speed of 750 rpm. The titration consisted of 19 injections of 2 µL each, separated by 150 s equilibration intervals. Data analysis was performed using Origin Pro software, fitting the data to a single-site binding model.

Soft Agar Motility Assay. *C. jejuni* strains were cultured on blood agar plates under microaerobic conditions at 37 °C for 24 h. Colonies were picked using a sterilized tip and stabbed onto semisolid *Brucella* broth plates containing 0.3% agar. These plates were then incubated microaerobically (85% N₂, 10% CO₂, 5% O₂) at 37 °C for 12 h.

Bioinformatic Analysis. For the search of FlgXc_j homologs in the phylum *Campylobacterota*, we first used the FlgX protein sequence from *C. jejuni* 81-176 as the query file to search against a local BLAST database composed of 82 genomes sequenced from the *Campylobacterota* (*SI Appendix, Table S1*). Due to the low sequence similarity of FlgX homologs, we set the BLAST parameters to E-value of 3.0. The retrieved FlgX homologs were present in various genera, except these four genera- *Arcobacter*, *Nitratifactor*, *Sulfurovum*, and *Nitratiruptor*. Additionally, due to the conserved gene order of *flgX* with upstream gene *ubiA*, which encodes a very conserved protein and is single copy in the genome, we also BLAST searched *ubiA* in all analyzed genomes of *Campylobacterota*. Then, the downstream gene of *ubiA* was analyzed by either HHpred or AlphaFold to verify whether it shows similarity to tPilZ-XCC6012.

To understand the evolution of FlgX in *Campylobacterota*, its homologs were mapped in a species tree showing the flagellation status and chemosensory classes collected from our recent studies (55). The species tree was constructed using the UBCG pipeline (63). Briefly, the tree was constructed based on sequence alignment of 92 single-copy concatenated marker proteins derived from the complete genomes of 82 species in *Campylobacterota*. Six closely related *Desulfurellales* species were used as the outgroup to root the tree.

Cryo-ET Sample Preparation. To prepare frozen-hydrated samples, the *C. jejuni* culture was centrifuged at 1,500×g for 10 min and resuspended with phosphate buffer saline (PBS) to a final OD₆₀₀ of 1.0. 10 nm of gold tracer solution (Aurion) was then added to the bacterial sample at a ratio of 1:1 (V/V). 5 μL of the mixture was deposited on the carbon side of discharged cryo-EM grids at room temperature. The backs of grids were then blotted with filter paper (Whatman™) for almost 4 s and immediately plunged into liquid ethane/propane mixture using a manual gravity plunger as described previously (31). We also prepared cryo-EM samples with Leica EM GP2 plunger. GP2 environmental chambers were set to 25 °C and 95% humidity. 5 μL of the *C. jejuni* culture was applied to the carbon side of the discharged cryo-EM grids. The grids were then blotted for 6 s and immediately plunge frozen in liquid ethane and propane mixture.

Cryo-ET Data Collection. Frozen-hydrated specimens of *C. jejuni* were imaged below −180 °C using the Titan Krios G2 300 kV transmission electron microscope (ThermoFisher) equipped with a field emission gun, K3 direct detection camera (Gatan), and GIF BioQuantum imaging Filter (Gatan). Tilt series data were collected using SerialEM software in the low-dose mode (64), and images were recorded at 42,000× magnification with a physical pixel size of 2.148 Å and 4.9 to 5.6 μm defocus. The angle of the tilt series ranged from −48° to +48° in increments of 3°, and the stage was tilted with the dose-symmetric scheme in FastTomo script (65). The total electron dose was ~65e[−]/Å² distributed across 33 images, and 10 frames of each image were recorded using the dose fraction mode in SerialEM. To generate whole 3D *C. jejuni* cell reconstructions, the same Krios G2 and SerialEM settings were used except for magnification and defocus. Images of the tilt series were recorded at 19,500× magnification with a physical pixel size of 4.556 Å and −6 μm defocus. Parameter of cryo-ET data acquisition and subtomogram averaging were summarized in *SI Appendix, Table S4*.

Reconstruction of Tomograms. Image drifting induced by the electron beam was corrected by MotionCor2 (66). IMOD software was used to create image stacks and align all images in each tilt series by tracking with fiducial beads (67, 68). Defocus for all images in the aligned tilt series was estimated using Gctf (69), and contrast transfer function (CTF) was corrected using the ctfphaseflip function in IMOD (70). The binvol function was used to generate 6× binning of the aligned stacks, and 6× binned tomograms with Simultaneous Iterative Reconstruction Technique (SIRT) were then reconstructed using Tomo3D (71). In total, 216, 193, and 109 tomograms were reconstructed from *C. jejuni* wild type, Δ*flgX*, and Δ*motA*, respectively.

Subtomogram Averaging of *C. jejuni* Flagellar Motors. Flagellar motors at the bacterial poles from 6× binned tomograms with SIRT reconstruction were manually picked using the tomopick command in i3 software package (72–74). In total, 265, 196, and 124 flagellar motors were selected from wild type, Δ*flgX*, and Δ*motA*, respectively. 6× binned reconstructed tomograms with weighted back projection (WBP) and i3 software package were used to determine initial averaged structures (72–74). For further structural analysis, subtomograms were extracted based on aligned positions of flagellar motors. Then, 4× and 2× binned subtomograms were extracted to perform 3D classification and refinement of the intact motor structures. To further improve the structural details of the stator complex and its interactions with other flagellar components, we used 17-fold symmetry expansion and focused refinement of the stator complex region. 1× binned subtomograms were then used to resolve the detailed interactions between the stator complex and FlgX.

Molecular Modeling of FlgX and Its Interactions with the Stator Complex. UCSF ChimeraX (75, 76) was used to segment electron density maps of the stator complex, FlgX, and connector from the in situ structure determined by

subtomogram averaging and focused refinement (Fig. 4H). AlphaFold3 was used to predict a model of the FlgX–MotA complex of *C. jejuni* (*SI Appendix, Fig. S7A*) (77). The MotA pentamer fits well into the MotA density region while the predicted FlgX tetramer model does not match with the two half rings (*SI Appendix, Fig. S7*). We rebuilt the FlgX tetramer model based on the densities from the two half rings under the MotA pentamer (*SI Appendix, Fig. S7C*). MotB from *B. burgdorferi* (32) and cryo-EM structure of the *S. Typhimurium* C-ring (PDB: 8uox) (20) were also used for the modeling (Fig. 5).

3D Visualization of an Intact Bacterium and Its Polar Flagella. IMOD (70) was used for 3D visualization of an intact *C. jejuni* cell and its polar flagella. The IMOD “Object” function was used to create contours of the outer membrane (OM), inner membrane (IM), and flagella, followed by “Meshing” function to construct mesh files. The flagellar motor components were segmented and visualized by using UCSF ChimeraX (75, 76).

Data, Materials, and Software Availability. The cryo-ET maps of the motor in *C. jejuni* WT, Δ*flgX*, and Δ*motA* mutant cells have been deposited in the Electron Microscopy Data Bank under accession codes EMD-45507 (78), EMD-45508 (79), and EMD-45509 (80), respectively (81). All other data are included in the manuscript and/or *SI Appendix*.

ACKNOWLEDGMENTS. We would like to thank Drs. Jianchao Li and Ran He from South China University of Technology for the SEC-MALS usage; Dr. Wei Xie and Hui Zhao from Sun-Yat-sen University for the ITC usage; Aijun Sun from South China Sea Institute of Oceanology, Chinese Academy of Sciences for her help during the CD analyses. In addition, we thank the High-Performance Computing Division at the South China Sea Institute of Oceanology for data analysis. We also thank Jack Botting (Yale University) for discussions about FlgX modeling and Jennifer Aronson (Yale University) for editing and valuable comments on the manuscript. This research was supported by the Open Fund of Nansha Islands Coral Reef Ecosystem National Observation and Research Station (NSICR23104), National Key Research and Development Program of China (2022YFC3102003), National Natural Science Foundation of China (32100097 and 32200101), the Science and Technology Planning Project of Guangdong Province of China (2021B1212050023), Key Special Project for Introduced Talents Team of Southern Marine Science and Engineering Guangdong Laboratory (Guangzhou) (GML2019ZD0407), and Innovation Academy of South China Sea Ecology and Environmental Engineering, Chinese Academy of Sciences (NO. ISEE2021ZD03 and ISEE2021PY05). S.T. and J.L. were supported by grants R01AI087946 and R01AI132818 from the National Institute of Allergy and Infectious Diseases; cryo-ET data were collected at Yale CryoEM Resource, which was funded in part by the NIH grant 1S10OD023603-01A1. We thank the Yale Center for Research Computing for guidance and use of the research computing infrastructure. H.Z. was supported by funds from the State Key Laboratory of Crop Stress Adaptation and Improvement of Henan University.

Author affiliations: ^aChinese Academy of Sciences Key Laboratory of Tropical Marine Bio Resources and Ecology, Guangdong Key Laboratory of Marine Materia Medica, Innovation Academy of South China Sea Ecology and Environmental Engineering, Guangdong Provincial Observation and Research Station for Coastal Upwelling Ecosystem, South China Sea Institute of Oceanology, Chinese Academy of Sciences, Guangzhou 511458, China; ^bSanya National Marine Ecosystem Research Station, Tropical Marine Biological Research Station in Hainan, Chinese Academy of Sciences, Sanya 572000, China; ^cSouthern Marine Science and Engineering Guangdong Laboratory (Guangzhou), Guangzhou 511458, China; ^dUniversity of Chinese Academy of Sciences, Beijing 100049, China; ^eDepartment of Microbial Pathogenesis, Yale School of Medicine, New Haven, CT 06536; ^fMicrobial Sciences Institute, Yale University, West Haven, CT 06516; and ^gState Key Laboratory of Crop Stress Adaptation and Improvement, School of Life Sciences, Henan University, Kaifeng 475004, China

1. N. Wadhwa, H. C. Berg, Bacterial motility: Machinery and mechanisms. *Nat. Rev. Microbiol.* **20**, 161–173 (2022).
2. H. Hu *et al.*, Structural basis of torque generation in the bi-directional bacterial flagellar motor. *Trends Biochem. Sci.* **47**, 160–172 (2022).
3. M. Rieu, R. Krutyholowa, N. M. I. Taylor, R. M. Berry, A new class of biological ion-driven rotary molecular motors with 5:2 symmetry. *Front. Microbiol.* **13**, 948383 (2022).
4. M. Santiveri *et al.*, Structure and function of stator units of the bacterial flagellar motor. *Cell* **183**, 244–257.e16 (2020).
5. J. C. Deme *et al.*, Structures of the stator complex that drives rotation of the bacterial flagellum. *Nat. Microbiol.* **5**, 1553–1564 (2020).
6. H. Celia *et al.*, Structural insight into the role of the Ton complex in energy transduction. *Nature* **538**, 60–65 (2016).
7. D. P. Williams-Jones *et al.*, Tunable force transduction through the Escherichia coli cell envelope. *Proc. Natl. Acad. Sci. U.S.A.* **120**, e2306707120 (2023).
8. R. Hennell James, J. C. Deme, A. Hunter, B. C. Berks, S. M. Lea, Structures of the type IX secretion/ gliding motility motor from across the phylum Bacteroidetes. *mBio* **13**, e0026722 (2022).
9. B. Nan *et al.*, Flagella stator homologs function as motors for myxobacterial gliding motility by moving in helical trajectories. *Proc. Natl. Acad. Sci. U.S.A.* **110**, E1508–E1513 (2013).
10. H. H. Hu *et al.*, Structure and mechanism of Zorya anti-phage defense system. *bioRxiv* [Preprint] (2024). <https://doi.org/10.1101/2023.12.18.572097> (Accessed 15 March 2024).

11. A. C. Ratliff, S. K. Buchanan, H. Celia, The Ton motor. *Front. Microbiol.* **13**, 852955 (2022).
12. J. Szczepaniak, C. Press, C. Kleantous, The multifarious roles of Tol-Pal in Gram-negative bacteria. *FEMS Microbiol. Rev.* **44**, 490–506 (2020).
13. M. J. McBride, Bacteroidetes gliding motility and the type IX secretion system. *Microbiol. Spectr.* **7**, 363–374 (2019).
14. G. Fu *et al.*, MotAB-like machinery drives the movement of MreB filaments during bacterial gliding motility. *Proc. Natl. Acad. Sci. U.S.A.* **115**, 2484–2489 (2018).
15. Y. Chang, B. L. Carroll, J. Liu, Structural basis of bacterial flagellar motor rotation and switching. *Trends Microbiol.* **29**, 1024–1033 (2021).
16. M. Homma, H. Terashima, H. Koiwa, S. Kojima, Putative spanner function of the Vibrio PomB plug region in the stator rotation model for flagellar motor. *J. Bacteriol.* **203**, e0015921 (2021).
17. Y. Chang *et al.*, Structural insights into flagellar stator-rotor interactions. *Elife* **8**, e48979 (2019).
18. Y. Chang *et al.*, Molecular mechanism for rotational switching of the bacterial flagellar motor. *Nat. Struct. Mol. Biol.* **27**, 1041–1047 (2020).
19. B. L. Carroll *et al.*, The flagellar motor of Vibrio alginolyticus undergoes major structural remodeling during rotational switching. *Elife* **9**, e61446 (2020).
20. S. Johnson *et al.*, Structural basis of directional switching by the bacterial flagellum. *Nat. Microbiol.* **9**, 1282–1292 (2024), 10.1038/s41564-024-01630-z.
21. P. K. Singh *et al.*, CryoEM structures reveal how the bacterial flagellum rotates and switches direction. *Nat. Microbiol.* **9**, 1271–1281 (2024), 10.1038/s41564-024-01674-1.
22. M. Kaplan *et al.*, The presence and absence of periplasmic rings in bacterial flagellar motors correlates with stator type. *Elife* **8**, e43487 (2019).
23. M. Beeby *et al.*, Diverse high-torque bacterial flagellar motors assemble wider stator rings using a conserved protein scaffold. *Proc. Natl. Acad. Sci. U.S.A.* **113**, E1917–E1926 (2016).
24. Z. Qin, W. T. Lin, S. Zhu, A. T. Franco, J. Liu, Imaging the motility and chemotaxis machineries in Helicobacter pylori by cryo-electron tomography. *J. Bacteriol.* **199**, e00695-16 (2017).
25. S. Zhu *et al.*, Molecular architecture of the sheathed polar flagellum in Vibrio alginolyticus. *Proc. Natl. Acad. Sci. U.S.A.* **114**, 10966–10971 (2017).
26. N. Takekawa, S. Kojima, M. Homma, Mutational analysis and overproduction effects of MotX, an essential component for motor function of Na⁺-driven polar flagella of Vibrio. *J. Biochem.* **161**, 159–166 (2017).
27. S. Zhu, T. Nishikino, S. Kojima, M. Homma, J. Liu, The Vibrio H-Ring facilitates the outer membrane penetration of the polar sheathed flagellum. *J. Bacteriol.* **200**, e00387-18 (2018).
28. Y. Chang, H. Xu, M. A. Motaleb, J. Liu, Characterization of the flagellar collar reveals structural plasticity essential for spirochete motility. *Mol. Biol.* **12**, e0249421 (2021).
29. K. H. Moon, X. Zhao, H. Xu, J. Liu, M. A. Motaleb, A tetratricopeptide repeat domain protein has profound effects on assembly of periplasmic flagella, morphology and motility of the Lyme disease spirochete Borrelia burgdorferi. *Mol. Microbiol.* **110**, 634–647 (2018).
30. H. Xu, J. He, J. Liu, M. A. Motaleb, BB0326 is responsible for the formation of periplasmic flagellar collar and assembly of the stator complex in Borrelia burgdorferi. *Mol. Microbiol.* **113**, 418–429 (2020).
31. S. Tachiyama *et al.*, The flagellar motor protein Flil forms a scaffold of circumferentially positioned rings required for stator activation. *Proc. Natl. Acad. Sci. U.S.A.* **119**, e2118401119 (2022).
32. S. Guo, H. Xu, Y. Chang, M. A. Motaleb, J. Liu, Flil ring enhances the function of periplasmic flagella. *Proc. Natl. Acad. Sci. U.S.A.* **119**, e2117245119 (2022).
33. M. Beeby, J. L. Ferreira, P. Tripp, S. V. Albers, D. R. Mitchell, Propulsive nanomachines: The convergent evolution of archaea, flagella and cilia. *FEMS Microbiol. Rev.* **44**, 253–304 (2020).
34. A. Boehm *et al.*, Second messenger-mediated adjustment of bacterial swimming velocity. *Cell* **141**, 107–116 (2010).
35. S. Subramanian, X. Gao, C. E. Dann III, D. B. Kearns, MotI (DgrA) acts as a molecular clutch on the flagellar stator protein MotA in Bacillus subtilis. *Proc. Natl. Acad. Sci. U.S.A.* **114**, 13537–13542 (2017).
36. B. Gao, M. Lara-Tejero, M. Lefebvre, A. L. Goodman, J. E. Galan, Novel components of the flagellar system in epsilonproteobacteria. *mBio* **5**, e01349-14 (2014).
37. D. A. Ribardo, B. R. Kelley, J. G. Johnson, D. R. Hendrixson, A chaperone for the stator units of a bacterial flagellum. *mBio* **10**, e01732-19 (2019).
38. M. Y. Galperin, S. H. Chou, Structural conservation and diversity of PilZ-related domains. *J. Bacteriol.* **202**, e00664-19 (2020).
39. Q. W. Cheang, L. Xin, R. Y. F. Chea, Z. X. Liang, Emerging paradigms for PilZ domain-mediated C-di-GMP signaling. *Biochem. Soc. Trans.* **47**, 381–388 (2019).
40. S. Kojima, T. Yoneda, W. Morimoto, M. Homma, Effect of PilZD, a YcgR homologue of c-di-GMP-binding protein, on polar flagellar motility in Vibrio alginolyticus. *J. Biochem.* **166**, 77–88 (2019).
41. A. E. Baker *et al.*, PilZ domain protein FlgZ mediates cyclic di-GMP-Dependent swarming motility control in Pseudomonas aeruginosa. *J. Bacteriol.* **198**, 1837–1846 (2016).
42. K. Paul, V. Nieto, W. C. Carlquist, D. F. Blair, R. M. Harshey, The c-di-GMP binding protein YcgR controls flagellar motor direction and speed to affect chemotaxis by a “backstop brake” mechanism. *Mol. Cell* **38**, 128–139 (2010).
43. L. Xu *et al.*, A cyclic di-GMP-binding adaptor protein interacts with a chemotaxis methyltransferase to control flagellar motor switching. *Sci. Signal.* **9**, ra102 (2016).
44. A. Pecina *et al.*, The stand-alone PilZ-domain protein MotL specifically regulates the activity of the secondary lateral flagellar system in Shewanella putrefaciens. *Front. Microbiol.* **12**, 668892 (2021).
45. T. N. Li *et al.*, A novel tetrameric PilZ domain structure from xanthomonads. *PLoS One* **6**, e22036 (2011).
46. B. J. Laventie *et al.*, Capture compound mass spectrometry—a powerful tool to identify novel c-di-GMP effector proteins. *J. Vis. Exp.* **97**, 51404 (2015), 10.3791/51404.
47. R. Mo, Y. Liu, Y. Chen, Y. Mao, B. Gao, Evolutionary principles of bacterial signaling capacity and complexity. *mBio* **13**, e0076422 (2022).
48. D. A. Ribardo, J. J. Johnson, D. R. Hendrixson, Viscosity-dependent determinants of Campylobacter jejuni impacting the velocity of flagellar motility. *mBio* **15**, e0254423 (2024).
49. T. Drobníček *et al.*, Molecular model of a bacterial flagellar motor in situ reveals a “parts-list” of protein adaptations to increase torque. *bioRxiv* [Preprint] (2023). <https://doi.org/10.1101/2023.09.08.556779> (Accessed 12 September 2023).
50. R. De Mot, J. Vanderleyden, The C-terminal sequence conservation between OmpA-related outer membrane proteins and MotB suggests a common function in both gram-positive and gram-negative bacteria, possibly in the interaction of these domains with peptidoglycan. *Mol. Microbiol.* **12**, 333–334 (1994).
51. S. Kojima *et al.*, Stator assembly and activation mechanism of the flagellar motor by the periplasmic region of MotB. *Mol. Microbiol.* **73**, 710–718 (2009).
52. A. Roujeinikova, Crystal structure of the cell wall anchor domain of MotB, a stator component of the bacterial flagellar motor: Implications for peptidoglycan recognition. *Proc. Natl. Acad. Sci. U.S.A.* **105**, 10348–10353 (2008).
53. L. L. Sharp, J. Zhou, D. F. Blair, Tryptophan-scanning mutagenesis of MotB, an integral membrane protein essential for flagellar rotation in Escherichia coli. *Biochemistry* **34**, 9166–9171 (1995).
54. L. L. Sharp, J. Zhou, D. F. Blair, Features of MotA proton channel structure revealed by tryptophan-scanning mutagenesis. *Proc. Natl. Acad. Sci. U.S.A.* **92**, 7946–7950 (1995).
55. R. Mo *et al.*, The evolutionary path of chemosensory and flagellar macromolecular machines in Campylobacterota. *PLoS Genet.* **18**, e1010316 (2022).
56. V. M. Gumerov, E. P. Andrianova, I. B. Zhulin, Diversity of bacterial chemosensory systems. *Curr. Opin. Microbiol.* **61**, 42–50 (2021).
57. L. K. Lee, M. A. Ginsburg, C. Crovace, M. Donohoe, D. Stock, Structure of the torque ring of the flagellar motor and the molecular basis for rotational switching. *Nature* **466**, 996–1000 (2010).
58. G. Cha, Z. Chen, R. Mo, G. Lu, B. Gao, The novel regulators CheP and CheQ control the core chemotaxis operon cheVAW in Campylobacter jejuni. *Mol. Microbiol.* **111**, 145–158 (2019).
59. D. G. Gibson *et al.*, Enzymatic assembly of DNA molecules up to several hundred kilobases. *Nat. Methods* **6**, 343–345 (2009).
60. J. Jumper *et al.*, Highly accurate protein structure prediction with AlphaFold. *Nature* **596**, 583–589 (2021).
61. M. Mirdita *et al.*, ColabFold: Making protein folding accessible to all. *Nat. methods* **19**, 679–682 (2022).
62. F. Gabler *et al.*, Protein sequence analysis using the MPI bioinformatics toolkit. *Curr. Protoc. Bioinformatics* **72**, e108 (2020).
63. S. I. Na *et al.*, UBCG: Up-to-date bacterial core gene set and pipeline for phylogenomic tree reconstruction. *J. Microbiol.* **56**, 280–285 (2018), 10.1007/s12275-018-8014-6.
64. D. N. Mastronarde, Automated electron microscope tomography using robust prediction of specimen movements. *J. Struct. Biol.* **152**, 36–51 (2005).
65. A. Xu, C. Xu, FastTomo: A SerialEM script for collecting electron tomography data. *bioRxiv* [Preprint] (2021). <https://doi.org/10.1101/2021.03.16.435675> (Accessed 20 December 2023).
66. S. Q. Zheng *et al.*, MotionCor2: Anisotropic correction of beam-induced motion for improved cryo-electron microscopy. *Nat. Methods* **14**, 331–332 (2017).
67. J. R. Kremer, D. N. Mastronarde, J. R. McIntosh, Computer visualization of three-dimensional image data using IMOD. *J. Struct. Biol.* **116**, 71–76 (1996).
68. D. N. Mastronarde, S. R. Held, Automated tilt series alignment and tomographic reconstruction in IMOD. *J. Struct. Biol.* **197**, 102–113 (2017).
69. K. Zhang, Gctf: Real-time CTF determination and correction. *J. Struct. Biol.* **193**, 1–12 (2016).
70. Q. Xiong, M. K. Morpheus, C. L. Schwartz, A. H. Hoenger, D. N. Mastronarde, CTF determination and correction for low dose tomographic tilt series. *J. Struct. Biol.* **168**, 378–387 (2009).
71. J. I. Agulleiro, J. J. Fernandez, Tomo3D 2.0—exploitation of advanced vector extensions (AVX) for 3D reconstruction. *J. Struct. Biol.* **189**, 147–152 (2015).
72. D. R. Morado, B. Hu, J. Liu, Using Tomoauto: A protocol for high-throughput automated cryo-electron tomography. *J. Vis. Exp.* **107**, e53608 (2016), 10.3791/53608.
73. H. Winkler *et al.*, Tomographic subvolume alignment and subvolume classification applied to myosin V and SIV envelope spikes. *J. Struct. Biol.* **165**, 64–77 (2009).
74. H. Winkler, 3D reconstruction and processing of volumetric data in cryo-electron tomography. *J. Struct. Biol.* **157**, 126–137 (2007).
75. T. D. Goddard *et al.*, UCSF ChimeraX: Meeting modern challenges in visualization and analysis. *Protein Sci.* **27**, 14–25 (2018).
76. E. F. Pettersen *et al.*, UCSF ChimeraX: Structure visualization for researchers, educators, and developers. *Protein Sci.* **30**, 70–82 (2021).
77. J. Abramson *et al.*, Accurate structure prediction of biomolecular interactions with AlphaFold 3. *Nature* **630**, 493–500 (2024), 10.1038/s41586-024-07487-w.
78. S. Tachiyama, H. Zhao, J. Liu, In situ structure of C. jejuni flagellar motor. EMBD. <https://www.ebi.ac.uk/emdb/EMD-45507>. Deposited 22 July 2024.
79. S. Tachiyama, H. Zhao, J. Liu, In situ structure of Campylobacter jejuni flagellar motor from flgX deletion mutant. EMBD. <https://www.ebi.ac.uk/emdb/EMD-45508>. Deposited 22 July 2024.
80. S. Tachiyama, H. Zhao, J. Liu, In situ structure of C. jejuni flagellar motor from motA deletion mutant. EMBD. <https://www.ebi.ac.uk/emdb/EMD-45509>. Deposited 22 July 2024.
81. The wwPDB Consortium, EMD—the Electron Microscopy Data Bank. Nucleic Acids Research. <https://doi.org/10.1093/nar/gkad1019>. Deposited 22 July 2024.